URSI GASS 2026, Krakow, Poland, 15 – 22 August 2026

Machine Learning-Assisted Prediction of Spherical Harmonics and Application to the Synthesis of Accurate MIMO Radar Patterns

Nehir Berk Onat, Tworit Dash, Alexander Yarovoy, and Yanki Aslan
Department of Microelectronics, Delft University of Technology, The Netherlands

Abstract

A novel spherical-harmonics-based embedded element pattern (EEP) prediction technique is proposed to address the open challenge of efficient and error-robust pattern prediction in aperiodic arrays. The method enables mutual-coupling (MC)-aware synthesis of multiple-input multiple-output (MIMO) radar patterns. A neural network (NN) predicts the spherical mode coefficients, from which the antenna-under-test (AUT) field patterns are reconstructed for candidate topologies. The trained models are integrated into a particle swarm optimization (PSO) framework for MIMO array topology optimization, targeting minimization of the maximum side-lobe level (SLL). The synthesized patterns are validated against full-wave simulation results.

1 Introduction

Irregular MIMO antenna arrays are widely used in high-resolution radar sensing [1], yet most synthesis methods optimize sidelobe levels while neglecting mutual coupling [2]. Ignoring resulting EEP variations causes significant mismatch between optimized and realized patterns, degrading sensing performance [3]. Although full-wave optimization can address this for small arrays, it is computationally prohibitive for large or complex designs.

While machine learning (ML) enables electromagnetic response prediction, existing array-level methods suffer from dataset dependency or numerical instability [4, 5]. Consequently, robust EEP prediction and MC-aware ML-assisted MIMO radar synthesis remain largely unexplored. This paper introduces a spherical-harmonics-based EEP prediction method with superior accuracy and robustness, and presents the first MC-aware optimization framework for MIMO radar pattern synthesis. The paper is organized as follows: Section II formulates the problem, Sections III and IV describe the proposed NN and optimization framework, Section V presents results, and Section VI concludes.

2 Problem Formulation

2.1 Antenna Under Test (AUT)

This work considers a K-element irregularly spaced pin-fed circular patch array operating at 10 GHz. Fig. 1 illustrates an example array topology, and the key design parameters are provided in Table 1. The aim is to predict the EEP of the AUT, which is positioned at the origin, while the surrounding elements are randomly placed within a specified region, constrained by an inner and an outer circle. The inner circle has a radius of $r_1 = 0.5\lambda$, where λ is the wavelength. The outer circle has a radius of $r_2 = \lambda$, ensuring that the MC effects on the EEPs can be analyzed by maintaining close element spacing. To preserve a quasi-random distribution, the minimum allowable separation between elements is set at 0.5λ. Furthermore, each EEP in the topology can be found by changing the AUT among the elements.

The far-field virtual array pattern of a MIMO radar placed on the yz plane is found as:

$$E_M(\theta,\phi) = \sum_{k_t,k_r=1}^{K_t,K_r} E_{k_t}^{TX}(\theta,\phi) E_{k_r}^{RX}(\theta,\phi) \mathrm{e}^{\mathrm{j}2\pi/\lambda (y_{k_r}^{k_t}\sin\theta\sin\phi + z_{k_r}^{k_t}\cos\theta)}, \quad (1)$$

where λ is the wave length, $E_{k_t}^{TX}(\theta,\phi)$ and $E_{k_r}^{RX}(\theta,\phi)$ are the EEP of the k_t-th and k_r-th element in TX and RX topologies, respectively, where the EEPs of the TX topology are taken as isolated element pattern (IEP) due to the high sparsity. Furthermore, $y_{k_r}^{k_t}$ and $z_{k_r}^{k_t}$ are superposition of the TX and RX positions and can be found as $y_{k_r}^{k_t} = y_{k_t} + y_{k_r}$ and $z_{k_r}^{k_t} = z_{k_t} + z_{k_r}$, respectively. It is worth to note that (1) assumes that the array does not utilize any amplitude tapering.

2.2 Spherical Harmonics

The EEP far-field patterns, given in (1), can be decomposed into modes of spherical harmonics, which are considered

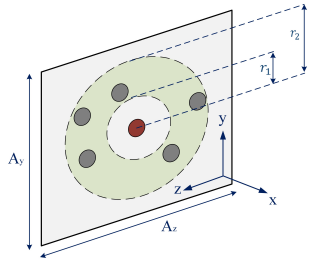


Figure 1. K = 6-element aperiodic array where the AUT is located at the center, and the neighboring elements are randomly positioned in the region: $r_1^2 \le (y_i^2 + z_i^2) \le r_2^2$ where (y_i, z_i) is the location of the i-th neighbor element in λ.

Table 1. Antenna design parameters

Center frequency	10 GHz	**Aperture length** (A_y)	2λ
Patch radius	4.44 mm	**Aperture width** (A_z)	2λ
Feeding type	pin-fed	**Substrate height** (h)	0.41 mm
Circle rad. [r_1,r_2]	$[0.5,1]\lambda$	**Permittivity** (ε_r)	3.55

the basis functions. The absolute value of the electric field can be represented as a weighted sum [6]:

$$|E(\theta,\phi)| = \sum_{l=0}^{\infty}\sum_{m=-l}^{+l} c_l^m Y_l^m(\theta,\phi), \tag{2}$$

where

$$Y_l^m(\theta,\phi) = \sqrt{\frac{2l+1}{4\pi}\frac{(l-|m|)!}{(l+|m|)!}} P_l^{|m|}(\cos\theta)\exp(\mathrm{j}m\phi), \tag{3}$$
$$l \in [0,\infty], m \in [-l,+l],$$

where the numbers l, and m represent the mode indices, θ is the elevation angle, ϕ is the azimuth angle, P_l^m are the associated Legendre functions of lth degree (or level) and mth order (modes). The c_l^m in (2) are the complex weights of these modes. These modes are orthonormal, meaning that:

$$\int_\Omega Y_l^m(\theta,\phi) Y_{l'}^{m'}(\theta,\phi) d\Omega = \delta_{ll'}\delta_{mm'} \tag{4}$$

where δ is the Dirac delta function and Ω is the surface area. The (2) can be written with matrix form as:

$$|\mathbf{e}| = \mathbf{Y}\mathbf{c}, \tag{5}$$

where $\mathbf{Y}$ contains all the spherical wave mode basis functions $\mathbf{Y} = [\mathbf{y}_0^0, \mathbf{y}_1^{-1}, \mathbf{y}_1^0, \mathbf{y}_1^1, \cdots, \mathbf{y}_{L-1}^{L-1}]$ ($L-1$ being the highest degree, L being the number of degrees used). Each entry to this matrix $\mathbf{Y}$, i.e., $\mathbf{y}_l^m \in C^{(N_\theta N_\phi)\times 1}$ are vectorized form of the spherical modes (basis functions), where N_θ and N_ϕ are the number of elevation and azimuth directions, respectively. The matrix $\mathbf{Y} \in C^{(N_\theta N_\phi)\times L^2}$ is then a 2D matrix. Therefore, $\mathbf{c} \in C^{L^2\times 1}$, where $\mathbf{c} = [c_0^0, c_1^{-1}, c_1^0, c_1^1, \ldots, c_{L-1}^{L-1}]^{\mathrm{T}}$. Uppercase and lowercase bold fonts refer to matrices and vectors, respectively. Therefore, the vector $|\mathbf{e}| \in R^{(N_\theta N_\phi)\times 1}$.

2.3 EEP Far Field Reconstruction

If the noisy vectorized far-field measurement, $\mathbf{f} \in C^{(N_\theta N_\phi)\times 1}$, is given, the spherical wave mode coefficients are estimated using least squares:

$$\hat{\mathbf{c}} = \left(\mathbf{Y}^{\mathrm{H}}\mathbf{Y}\right)^{-1}\mathbf{Y}^{\mathrm{H}}\mathbf{f}, \tag{6}$$

where $\mathbf{Y}^\dagger = (\mathbf{Y}^{\mathrm{H}}\mathbf{Y})^{-1}\mathbf{Y}^{\mathrm{H}}$ is the Moore-Penrose inverse. This paper employs a *Singular Value Decomposition* (SVD)-based approach for computational efficiency and numerical stability via low-rank approximation. The basis function matrix $\mathbf{Y}$ (with independent columns) is decomposed as, and the coefficients are computed as:

$$\mathbf{Y} = \mathbf{U}\Sigma\mathbf{V}^{\mathrm{H}}, \quad \hat{\mathbf{c}} = \mathbf{V}\Sigma^{-1}\mathbf{U}^{\mathrm{H}}\mathbf{f}, \tag{7}$$

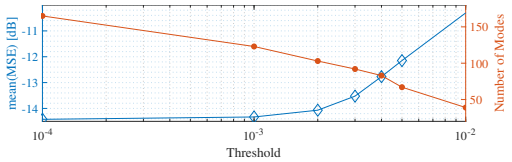


Figure 2. An example comparison plot showing the selected number of modes with a defined threshold for the absolute value of the coefficients, where MSE quantifies the error over the 4-element dataset comprising 4000 randomly generated topologies.

where $\mathbf{U} \in C^{(N_\theta N_\phi)\times 1}$, $\Sigma \in C^{L^2\times L^2}$ (a decaying diagonal matrix), and $\mathbf{V} \in C^{L^2\times L^2}$. The number of significant modes used is $L^2 = 169$ after manual investigation. After the coefficients are computed, the reconstruction of the absolute electric field can be determined using:

$$|\hat{\mathbf{e}}| = \mathbf{Y}\hat{\mathbf{c}}. \tag{8}$$

3 Significant Spherical Modes for EEP Prediction and the Proposed NN Architecture

Following the AUT topology in Fig. 1, the NN model takes the coordinates of neighboring elements in the defined region as input. Since the number of neighboring elements varies by topology, separate models are developed for each case. The trained models predict the spherical mode coefficients, $\hat{\mathbf{c}}$ in (6), of the AUT. Using a pre-calculated $\mathbf{Y}$, the AUT's field is reconstructed from the predicted coefficients. As discussed in Section 2.3, the number of significant modes is determined as $L^2 = 169$. Further reduction is possible by eliminating modes with near-zero values without compromising the field reconstruction performance. The optimal number of modes is selected based on dataset analysis to balance accuracy and efficiency. The reconstruction error is quantified using the MSE:

$$MSE = 10\log\left(\frac{1}{N_s^2}\sum^{N_s}(|\mathbf{e}| - |\hat{\mathbf{e}}|)^2\right) \tag{9}$$

where N_s is the total number of samples of the vector $\mathbf{e}$, which comprises the full-wave simulated electric field of the chosen element in the far-field region that is generated by the commercial full-wave simulator CST, $\hat{\mathbf{e}}$ is the reconstructed pattern in vector form as given in (8).

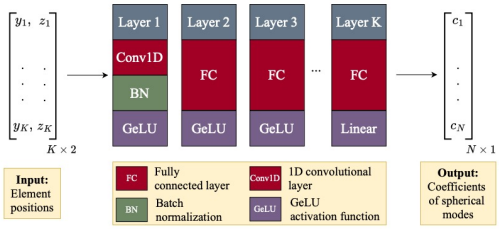


Figure 3. Block diagram of the proposed architecture. K: total number of neighbor element in the topology, N: number of considered modes. The number of layers increases linearly with the number of elements considered. After each layer, the GeLU activation function is applied, except in the final layer, where a linear activation is used.

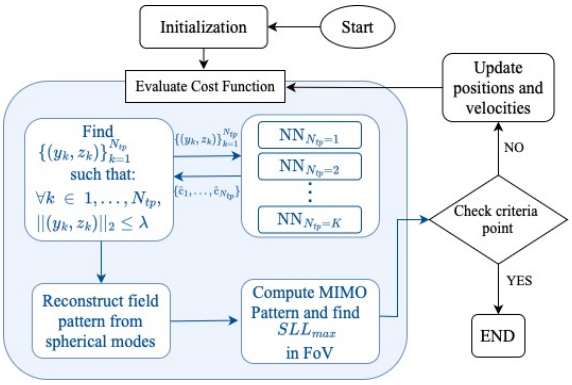


Figure 4. Utilized PSO framework where NN models are integrated into MATLAB. During cost function evolution, the NN models are called for each element depending on the number of neighbor elements in the defined circle, N_{tp}, to predict the spherical wave coefficients, $\hat{\mathbf{c}}$. The predicted coefficients are further used to reconstruct the EEP of the AUT. After predicting each EEP for a given topology, the MIMO virtual pattern is calculated, and the maximum SLL is found for each candidate solution.

The relation between the MSE, the chosen absolute threshold value for the coefficients, and the number of modes was investigated in each dataset to find the optimal number of modes. As each topology comprising a different number of elements shows a similar behavior, Fig. 2 illustrates this relation for the 4-element dataset comprising 4000 randomly generated topologies. The mean MSE and the number of modes are related inversely. With an increase in the threshold, the mean MSE increases, while the number of modes decreases (represented by the two lines in Fig. 2). The optimal compromise can be taken as the intersection of these two lines, which occurs at around 81 modes.

Since the estimation space consists of 81 complex coefficients, a relatively simple network can be used for prediction. The model begins with a 1D convolutional layer with 16 kernels to encode spatial information, followed by a fully connected layer that outputs an 81×2 matrix (real and imaginary parts). As the number of elements in the topology increases, the network depth grows to handle the increased prediction complexity. Initially, four fully connected layers are used after the convolutional layer, with neurons increasing up to 162. The number of layers and

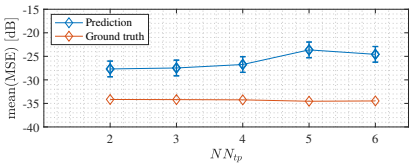


Figure 5. Mean MSE comparison over the test set: (red) between the full-wave simulated pattern and the reconstructed pattern using ground truth coefficients; (blue) between the full-wave simulated pattern and the reconstructed pattern using NN-predicted coefficients, with vertical lines indicating the standard deviation of the corresponding model, NN_{tp}.

Table 2. Maximum SLL Comparison Between NN-Assisted MIMO Topology Optimization and Full-Wave Simulation of the Optimized Pattern

Steering (θ_0, ϕ_0)	(0°,0°)	(0°,30°)	(0°,-30°)	(30°,0°)	(-30°,0°)
$max(SLL_{\text{NN}})$ [dB]	-18.03	-16.23	-16.03	-16.03	-16.09
$max(SLL_{\text{fw}})$ [dB]	-17.23	-16.67	-16.17	-15.56	-15.58
$max(SLL_{\text{IEP}})$ [dB]	-17.10	-15.36	-15.36	-13.10	-13.10

neurons was fine-tuned heuristically for each model. To prevent overfitting, dropout layers were introduced when the fully connected layers increased to six for the 5- and 6-element cases. Figure 3 illustrates an example architecture, where K represents the maximum number of neighboring elements, and N is the number of utilized modes, set to 81.

The network is trained using the ADAM optimizer with the default hyper parameters (η=0.001, β_1=0.9, β_2=0.999, ε=1e-7) and the MSE between the estimated and the true coefficients as loss function. Once the coefficients are predicted, the field can be reconstructed by using (8).

4 MIMO Radar Optimization Framework

Particle Swarm Optimizer (PSO) has been used to carry out the optimization routine for the synthesis problem. During the optimization process, the location of the array elements in TX and RX is simultaneously optimized to minimize the maximum side lobe level (SLL) in the defined field of view (FoV) for a multiple-beams scenario. Figure 4 illustrates the block diagram of the utilized PSO.

The approach proposed in Section 3 is integrated into the optimizer to achieve MC-aware synthesis. Each NN model is trained using TensorFlow in Python. For optimization, the trained models are integrated into MATLAB, leveraging its computational capabilities. In this way, the EEP of the elements are obtained in every iteration to compute the virtual array pattern of each candidate solution.

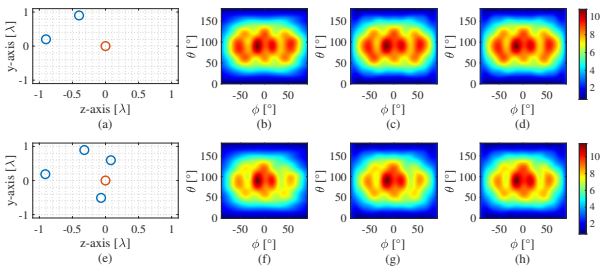


Figure 6. Example topology results for the 2- and 4-element neighboring cases are shown (electric fields in linear scale). (a) and (e) illustrate the array topologies, where the red circle represents the AUT and the blue circles represent the neighboring elements; (b) and (f) display the full-wave simulated patterns of the AUT for each case, respectively; (c) and (g) show the reconstructed patterns using the ground truth coefficients; (d) and (h) depict the reconstructed patterns using the NN-predicted coefficients.

5 Results

5.1 EEP Prediction via Spherical Modes

Five NN models were developed, each corresponding to a different number of neighboring elements. Models for 2–6 elements were designed, with the circular region in Fig. 1 constrained to λ, as discussed in Section III. For the single-element case, the isolated element pattern was assumed. For each configuration, 4000 quasi-randomly distributed samples were generated in CST, and the resulting far-field patterns were converted into spherical wave mode coefficients. Of the dataset, 80% was used for training, with the remaining data equally split between validation and testing.

Fig. 5 compares the mean MSE for two cases: (1) reconstruction using ground-truth coefficients and (2) reconstruction using NN-predicted coefficients. In most cases, the mean error remains below -25 dB, indicating high accuracy, while the standard deviation stays within 2 dB. As the number of elements exceeds four, the prediction errors increase due to the higher complexity of the problem; however, this can be mitigated with additional training data. Fig. 6 illustrates the 2- and 4-element cases, demonstrating the effect of neighboring elements on the AUT EEP. In both cases, the trained models accurately predict the coefficients, enabling high-fidelity field reconstruction.

5.2 Mutual Coupling-Aware Multi-Beam MIMO Radar Topology Optimization

The trained models in the previous section were integrated into the PSO to achieve accurate MIMO radar topology for multi-beam applications. The element positions of the TX and RX topologies comprising 6 and 8 elements, respectively, are optimized simultaneously. Furthermore, the FoV is limited to $45^\circ \leq \theta \leq 135^\circ$ and $-45^\circ \leq \phi \leq 45^\circ$. For this work, 5 different steering angle combinations are considered: $(\theta_o, \phi_o) = [(0^\circ, 0^\circ), (0^\circ, 30^\circ), (0^\circ, -30^\circ), (30^\circ, 0^\circ), (-30^\circ, 0^\circ)]$.

Table 2 summarizes the maximum SLL within the FoV for each beam in the optimized topologies, while Fig. 7 shows the corresponding TX and RX configurations. The proposed optimization achieves an average maximum SLL of -16 dB, and the full-wave simulation results agree well with the proposed methodology, whereas patterns generated using the IEP remain unreliable. Fig. 8 compares the far-field patterns of the virtual array for all steering angles with full-wave simulations. Errors are observed in some edge regions, indicating that prediction accuracy for corner elements can be further improved.

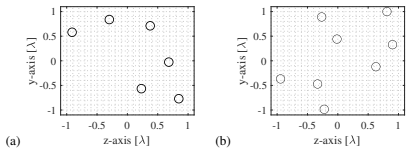


Figure 7. Optimized MIMO radar topologies: (a) TX topology with 6 elements; (b) RX topology with 8 elements.

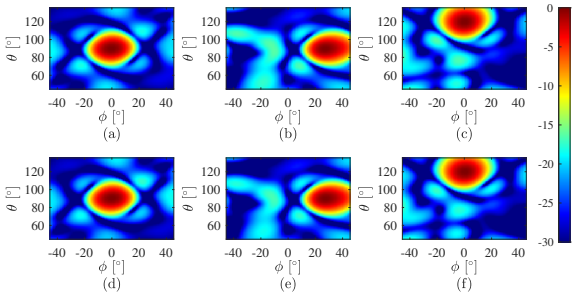


Figure 8. Optimized far-field patterns in the FoV and comparison with full-wave simulations (normalized, in [dB]). Top row is the optimized patterns with predicted EEPs and bottom row is the full-wave simulations. (a) and (d) are the boresight; (b) and (e) are steered by $(\theta_o = 0^\circ, \phi_o = 30^\circ)$; (c) and (f) are steered by $(\theta_o = 30^\circ, \phi_o = 0^\circ)$.

6 Conclusion

This paper proposed a novel NN-based EEP prediction method using spherical harmonics, enabling accurate reconstruction while considering MC effects. The approach was integrated into a PSO framework for MIMO radar topology optimization, effectively minimizing maximum SLL. Through the synthesis of an irregular MIMO radar topology comprising 6-element TX and 8-element RX, it is demonstrated that the proposed method offers a robust and efficient solution for MC-aware array synthesis, including multiple scanned beams in a given field of view.

References

[1] X. Zhuge and A. G. Yarovoy, "Study on Two-Dimensional Sparse MIMO UWB Arrays for High Resolution Near-Field Imaging," *IEEE Trans. Antennas Propag.*, **60**, 9, Sep. 2012, pp. 4173–4182.

[2] J. Wang, X. Wu, J. Ye, J. Sun, and G. Hua, "A Novel Two-Way Pattern Synthesis Method with the Uniform and Thinned Arrays," *IEEE Antennas Wireless Propag. Lett.*, **23**, 10, Oct. 2024, pp. 3108–3112.

[3] W. P. Keizer, "Planar Phased-Array Antennas: Mutual Coupling and Ultralow Peak Sidelobes," *IEEE Antennas Propag. Mag.*, **61**, 1, Feb. 2018, pp. 14–28.

[4] N. Onat, I. Roldan, F. Fioranelli, A. Yarovoy, and Y. Aslan, "Dataset Dependency of Data-Driven Machine Learning Techniques in Pattern Prediction under Mutual Coupling," in *Proc. 4th URSI Atlantic Radio Sci. Meeting (AT-RASC)*, 2024, pp. 1–4.

[5] N. B. Onat, I. Roldan, F. Fioranelli, A. Yarovoy, and Y. Aslan, "Constrained Infinitesimal Dipole Modeling-Assisted Ensemble Prediction of Embedded Element Patterns via Machine Learning," *IEEE Trans. Antennas Propag.*, **72**, 9, Sep. 2024, pp. 7353–7358.

[6] M. Costa, A. Richter, and V. Koivunen, "Unified Array Manifold Decomposition Based on Spherical Harmonics and 2-D Fourier Basis," *IEEE Trans. Signal Process.*, **58**, 9, Sep. 2010, pp. 4634–4645.